Astronomy & Astrophysics manuscript no. aanda
June 4, 2026

Predictions for the X-ray polarisation modulation in Cygnus X-1 from reflection off the stellar companion and its wind

Bert Vander Meulen[1,2], Kun Hu[3], Victoria Grinberg[1], and Henric Krawczynski[4]

[1] European Space Agency (ESA), European Space Research and Technology Centre (ESTEC), Keplerlaan 1, 2201 AZ Noordwijk, The Netherlands
e-mail: bert.vandermeulen@esa.int
[2] Department of Physics and Astronomy, Universiteit Gent, Proeftuinstraat 86 N3, B-9000 Ghent, Belgium
[3] Washington University in St. Louis, Physics Department, McDonnell Center for the Space Sciences, Brookings Dr. 1, 63130 St. Louis, MO, USA
[4] Washington University in St. Louis, Physics Department, McDonnell Center for the Space Sciences, and Center for Quantum Leaps, Brookings Dr. 1, 63130 St. Louis, MO, USA

Received June 4, 2026; accepted ...

ABSTRACT

Context. Cygnus X-1 is one of the brightest X-ray binaries, and has been observed multiple times with the Imaging X-ray Polarimetry Explorer (IXPE). Recent studies report tentative evidence for a polarisation modulation with the orbital period $P_{\rm orb}$, but a half-period ($P_{\rm orb}/2$) signal, expected from reflection off the companion star and its stellar wind, has not been reported.
Aims. We aim to quantify the reflection-induced variations of the polarisation degree PD and polarisation angle PA in Cygnus X-1 as a function of orbital phase and photon energy, and interpret these in terms of binary geometry and wind structure.
Methods. We set up a radiative transfer model combining a general relativistic description of the polarised X-ray source emission (kerrC) with a focussed stellar wind model for the binary medium. Using the 3D X-ray radiative transfer code SKIRT, we simulate broadband Stokes I, Q, and U fluxes, surface brightness maps, and linear polarisation maps over one binary orbit.
Results. We find a prominent double-peaked ($P_{\rm orb}/2$) polarisation modulation, with a peak-to-peak PD amplitude of 0.25, 0.81, and 1.24 percentage points in the $2-4$, $4-6$, and $6-8$ keV bands, respectively, with a strong energy dependence. The PA modulation is more modest, with $|\Delta\mathrm{PA}| < 4.6°$. Crucially, X-ray reprocessing reduces the overall PD relative to the intrinsic source polarisation.
Conclusions. The polarisation modulation is driven by reflection off the companion star and the focussed stellar wind, which induces a polarisation signal that alternately reinforces and counteracts the source polarisation throughout the orbit. The diffuse scattering halo surrounding the X-ray source drives no modulation, but systematically reduces the PD through its anisotropic illumination by the disk-corona system, an effect that should be accounted for in all wind-fed X-ray binaries. The PD amplitude increases with energy as photo-absorption disproportionately attenuates the distant-reflection signal; as the extinction drops, the reflection signal becomes increasingly important.

Key words. methods: numerical – polarisation – radiative transfer – X-rays: binaries – X-rays: individuals: Cygnus X-1

1. Introduction

The launch of the Imaging X-ray Polarimetry Explorer (IXPE) mission in 2021 has opened X-ray polarimetry as a new window on the high-energy Universe, enabling precise measurements of the linear polarisation degree PD and electric-field polarisation angle PA in the $2-8$ keV band, with PD sensitivities below 1% for bright Galactic and extragalactic sources (Weisskopf et al. 2022). Among IXPE's most prominent targets are black hole X-ray binaries (BHXRBs), for which significant polarisation has now been detected across hard, soft, and intermediate accretion states (see Rodriguez Cavero et al. 2023; Dovčiak et al. 2024; Majumder et al. 2026, for recent summaries of the observational IXPE results).

Cygnus X-1 (Cyg X-1) was the first BHXRB to be observed with IXPE (Krawczynski et al. 2022), being one of the brightest and best-studied X-ray sources in the sky (Jiang 2024). Cyg X-1 is a binary system consisting of a $21.2^{+2.2}_{-2.3}\,\mathrm{M}_\odot$ black hole and a $40.6^{+7.7}_{-7.1}\,\mathrm{M}_\odot$ O9.7 Iab supergiant companion star, HDE 226868, in a 5.6-day binary orbit viewed at $i = 27.5°^{+0.8°}_{-0.6°}$, at a distance of $2.22^{+0.18}_{-0.17}$ kpc (Miller-Jones et al. 2021, but see Ramachandran et al. 2025). The X-ray emission is powered by accretion of the strong stellar wind from the companion onto the black hole, and the wind structure can be probed through the phase-dependent absorption variability (e.g. Bałucińska-Church et al. 2000; Boroson & Vrtilek 2010; Grinberg et al. 2015; Yamada et al. 2025).

Cyg X-1 has since been observed multiple times with IXPE, and PD and PA have been measured with good accuracy in the hard (Krawczynski et al. 2022) and soft (Steiner et al. 2024) states, with $2-8$ keV polarisation degrees between 2% and 4%, and a polarisation direction that is aligned with the radio-jet axis. In both states, PD increases with energy across the IXPE band, while PA shows no significant energy dependence. The hard-state polarisation is consistent with Comptonisation in a hot corona extended in the accretion-disk plane, and suggests that the inner disk is viewed at a substantially higher inclination than the binary orbit. In the soft state, PD is a factor of two lower than the hard-state value, and polarisation may be attributed to returning radiation reflected off the accretion disk, constraining the black hole spin to $a \gtrsim 0.96$ (Krawczynski et al. 2022; Steiner et al. 2024, but alternative interpretations are discussed in Beloborodov 1998; Poutanen et al. 2023; Tomaru et al. 2024; Krawczynski & Hu 2025; Niedzwiecki et al. 2026).

Recently, Kravtsov et al. (2025) searched for time variability in the Cyg X-1 polarisation properties, scrutinising PD and PA for orbital variations with $P_{\rm orb}$ (i.e., 5.6 days; Gies et al. 2008) and longer-term, superorbital variability. The authors find tentative evidence for a 5.6-day modulation, which interestingly does not match the $P_{\rm orb}/2$ modulation expected from reflection off the companion star and its wind (Brown et al. 1978; Kravtsov et al. 2020, 2025; Rankin et al. 2024; Ahlberg et al. 2024). However, this $P_{\rm orb}/2$ signal may still be present at a level inaccessible with current observations, or could be masked by accretion-state-dependent polarisation changes.

This motivates a quantitative study of the reflection-induced PD and PA variations in Cyg X-1. In this work, we model X-ray reprocessing in the 3D binary system using the Monte Carlo radiative transfer code SKIRT (Vander Meulen et al. 2023, 2024), combining a general relativistic model for the polarised X-ray source emission (kerrC; Krawczynski & Beheshtipour 2022) with a 'focussed' stellar wind model that captures the essential geometry of the Cyg X-1 system (Gies & Bolton 1986b; Grinberg et al. 2015); in future work, this model will be refined by incorporating clumping and a more realistic asymmetric wind structure (Grinberg et al. 2015; Miškovičová et al. 2016). We predict how reflection off the companion star and its wind modulates PD and PA over one orbital period, and interpret the phase- and energy-dependence of the polarisation signal in terms of the system geometry. In a forthcoming paper, these predictions are confronted with the accumulated IXPE data.

The outline for this paper is as follows: In Sect. 2, we introduce the radiative transfer model, which comprises the kerrC source model (Sect. 2.1) and the binary system geometry (Sect. 2.2). The SKIRT implementation is described in Sect. 3, and the radiative transfer results are presented and discussed in Sect. 4. Our findings are summarised in Sect. 5.

2. Radiative transfer model

This work combines a general relativistic model for the polarised X-ray source emission from the disk-corona system (kerrC; Krawczynski & Beheshtipour 2022) with a geometric model for the binary system, comprising the companion star HDE 226868 and its focussed stellar wind (Grinberg et al. 2015). Both components are introduced in the following two subsections; their implementation in SKIRT is discussed in Sect. 3.

2.1. kerrC polarised source emission

kerrC is a general relativistic ray-tracing model to simulate and fit the X-ray flux and polarisation spectra (i.e., Stokes I, Q, and U) of accreting black hole systems (Krawczynski & Beheshtipour 2022). The model accounts for thermal emission emitted from a multi-temperature accretion disk and the subsequent Comptonisation within a hot corona. It also self-consistently includes the returning and reflected radiation. X-ray photons are ray-traced from the disk to a distant observer using a Kerr metric, and polarisation vectors are parallel transported along the photon geodesics. For a given set of black hole and corona parameters, kerrC calculates the flux and polarisation spectra for all viewing angles, which can be used to fit spectro-polarimetric observations of BHXRBs (see e.g. Krawczynski & Beheshtipour 2022; Krawczynski et al. 2022; West & Krawczynski 2023; Rodriguez Cavero et al. 2023; Marra et al. 2024; Steiner et al. 2024; Krawczynski et al. 2024; Awaki et al. 2025).

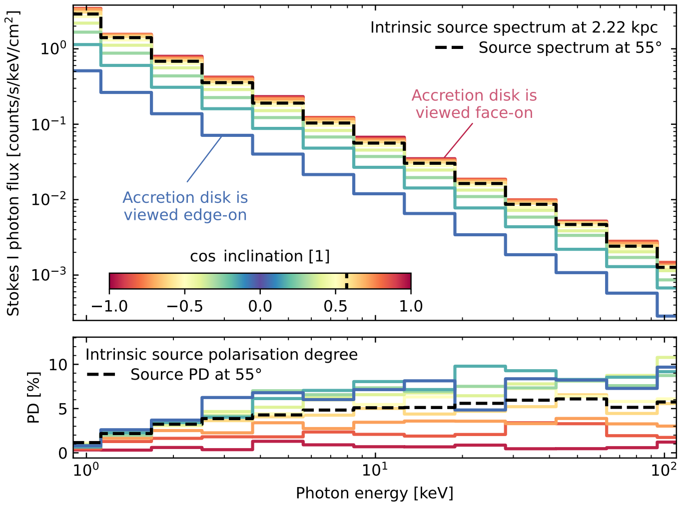

Fig. 1. Inclination-dependent polarised source emission from kerrC. Top: Stokes I photon flux spectrum for different inclinations relative to the accretion-disk axis. Bottom: Corresponding polarisation degree PD; the polarisation direction is always aligned with the projected accretion-disk axis (defined as PA = 0° in this work; Sect. 4.6). The direct source emission at 55° (black) corresponds to $i = 27.5°$ relative to the binary orbit (see text). The emission pattern is symmetric about the disk plane.

The adopted kerrC model for the primary X-ray emission of Cyg X-1 corresponds to a thin accretion disk surrounding a black hole with spin parameter $a = 0.95$, sandwiched by a wedge-shaped corona with a temperature of $kT = 100$ keV. We assume an opening angle of 10° for the corona and set the vertical optical depth to $\tau = 0.5$; the mass accretion rate is set to $3.5{\times}10^{13}$ kg s^{-1}. For these parameters, the kerrC flux spectrum at 55° (i.e., relative to the accretion-disk axis) matches Cyg X-1 in its hard state. Moreover, the corresponding polarisation is consistent with Cyg X-1 measurements from IXPE, finding a PD increasing from 4 to 6% in the 2 − 8 keV band, and *XL-Calibur*, finding a PD of about 5% in the 19 − 64 keV band (Krawczynski et al. 2022; Awaki et al. 2025), with a polarisation angle in the direction of the projected accretion-disk axis (defined as PA = 0° throughout this work; Sect. 4.6). Our kerrC model for the polarised X-ray source emission of Cyg X-1 is shown in Fig. 1.

The high PD measured by IXPE implies that the accretion disk is observed at a high viewing angle (~55°), which is substantially more edge-on than the binary orbit ($i = 27.5°$; Miller-Jones et al. 2021). This discrepancy could be reconciled by either invoking a relativistic outflowing corona, which would increase the polarisation degree at lower viewing angles (Beloborodov 1998; Poutanen et al. 2023), or by considering a misalignment between the accretion disk and the binary orbit (Krawczynski et al. 2022). The latter scenario is adopted in this work, but we stress that the polarisation variations induced by reflection within the binary system depend only weakly on the source model. We assume that the accretion disk is observed at a viewing angle of 55° (Fig. 1, black line), consistent with the best-fit kerrC model and recent XRISM results (Draghis et al. 2025). This implies a misalignment of $\Delta i = 27.5°$ between the accretion disk and the binary orbit (for which we adopt $i = 27.5°$).

2.2. Binary geometry with focussed wind

Before reaching the observer, the primary X-ray emission from the inner accretion flow (Sect. 2.1) is reprocessed within the binary system, by the supergiant companion star HDE 226868 and

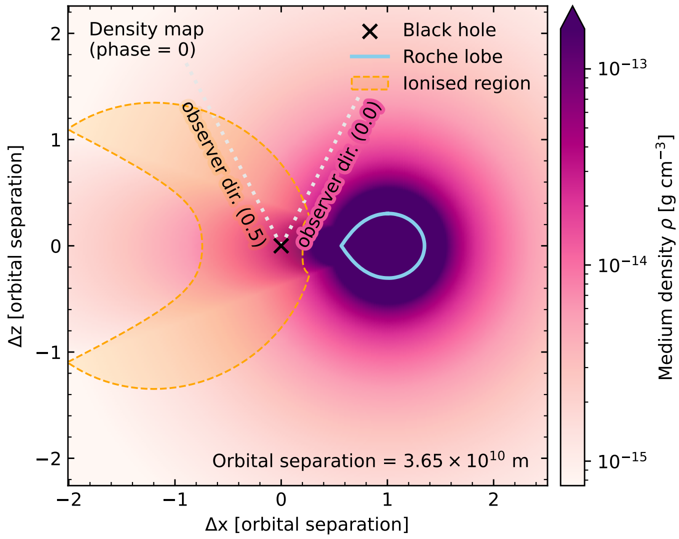

Fig. 2. Geometrical model for the Cyg X-1 binary system, comprising the black-hole X-ray source, the companion star, and a focussed stellar wind. The x-axis is the cylindrical symmetry axis connecting the black hole (centred on the origin) and the companion star (located at $x = 1$ in units of orbital separation). The ionised wind region is indicated in orange (see text). The binary system is observed at $i = 27.5°$ (Sect. 2.1); the observer directions at phases 0.0 and 0.5 are indicated in white.

its wind. The optically thick photosphere of the companion provides a large reflective surface, whose illuminated face rotates in and out of the line of sight over the binary orbit. The companion also drives a strong stellar wind (Castor et al. 1975), which permeates the system and constitutes an additional, extended scattering medium.

As HDE 226868 almost fills its Roche lobe (Gies et al. 2003; Ramachandran et al. 2025), the tidal forces exerted by the black hole focus the stellar wind towards the black hole, breaking the spherical symmetry and forming a density enhancement along the donor-black hole axis (Gies & Bolton 1986b,a; Sowers et al. 1998; Miller et al. 2005; Hanke et al. 2009; El Mellah et al. 2019; Brigitte et al. 2025). We model this with a smooth, axisymmetric wind model consisting of a spherical Castor-Abbott-Klein component (CAK; Castor et al. 1975) and a focussed wind stream directed towards the companion star (Friend & Castor 1982; Gies & Bolton 1986b,a), as shown in Fig. 2. Following Gies & Bolton (1986b), the focussed component occupies a conical region with an opening angle of 20°, where the wind is denser and slower than the CAK solution; outside this cone, the standard single-star CAK solution applies (see also Miškovičová et al. 2016). This model provides a good representation of the non-clumped wind in Cyg X-1 (Grinberg et al. 2015; Miškovičová et al. 2016), reproducing the observed optical (Gies & Bolton 1986b) and X-ray variability (Grinberg et al. 2015; Hirsch et al. 2019); in future work it will be refined to incorporate clumping (e.g. Owocki & Rybicki 1984; Sundqvist et al. 2018) and orbital deflections of the accretion stream (e.g. El Mellah et al. 2019).

We adopt the system parameters from Miller-Jones et al. (2021), updating the focussed-wind model employed in Grinberg et al. (2015) (see also Lai et al. 2024). Since the Gies & Bolton (1986b) wind model scales with system size, we obtain the same density distribution in units of orbital separation. However, as the updated separation of 3.65×10^{10} m exceeds the separation adopted in Grinberg et al. (2015) by a factor of 1.24, we rescale the volume density by 1/1.24 to preserve the observed $N_{\rm H}$ trend as a function of orbital phase. This density scaling is well within the uncertainties on the underlying mass-loss rate and wind velocity structure (Ramachandran et al. 2025). We note that the same procedure applies if alternative parameters are adopted: the density rescaling naturally recovers identical radiative transfer results, making our approach robust to ongoing revisions of the Cyg X-1 system parameters (e.g. Ramachandran et al. 2025).

The 2D density map of the binary system is shown in Fig. 2, representing the stellar companion and its wind. To obtain the 3D radiative transfer medium, this map must be revolved about the donor-black hole axis (i.e., the x-axis), which is the cylindrical symmetry axis of the system. Following Grinberg et al. (2015), we define two regions within the wind, assuming that Cyg X-1 is in the hard state: a highly ionised region close to the black hole, where the wind contributes to reflection but not absorption; and a more neutral region further away that contributes to both absorption and reflection. For details on the calculation of the ionised regions, readers can refer to Grinberg et al. (2015). Similarly, we rescale the threshold ionisation parameter $\xi_{\rm max}$ of Grinberg et al. (2015) by 1/1.24, to preserve the ionisation boundary in units of orbital separation, and thereby the observed absorption trend with orbital phase. The highly ionised wind region, corresponding to $\log \xi \geq 2.62$, is marked in orange on Fig. 2.

3. Radiative transfer setup

We employ the Monte Carlo radiative transfer code SKIRT[1] (Camps & Baes 2015, 2020; Vander Meulen et al. 2023, 2024) to propagate polarised kerrC source photons through the Cyg X-1 binary system, and predict the X-ray polarisation signal affected by reflection off the companion star and its wind. SKIRT models X-ray reprocessing in 3D, emulating photo-absorption with self-consistent fluorescent line emission and electron scattering, with full support for X-ray polarisation. For technical details, readers can refer to Vander Meulen et al. (2023, 2024).

In this study, two novel SKIRT features are deployed, which are introduced in Sect. 3.1 and Sect. 3.2. The general radiative transfer setup is described in Sect. 3.3.

3.1. kerrC source emission in SKIRT

The general-relativistic kerrC model (Sect. 2.1) provides the inclination-dependent flux and polarisation spectra of the X-ray source in Cyg X-1 (i.e., the inclination- and energy-dependent Stokes I, Q, and U parameters). To import these kerrC results to the SKIRT code, we introduced a new SKIRT function to model sub-grid source emission with an advanced emission pattern: the `FilePolarizedPointSource`[2].

The `FilePolarizedPointSource` class represents a single point source, emitting polarised radiation with an axisymmetric angular dependence, based on user-provided Stokes spectra that are tabulated as a function of inclination cosine. For this project, relevant configurable options are the location of the point source and the direction of the symmetry axis.

The kerrC Stokes spectra are provided for 18 linear cosine bins between −1 and 1, tabulated on a logarithmic energy grid with $E/\Delta E = 2.5$, covering the $1 - 200$ keV range. These tables are interpolated by the `FilePolarizedPointSource` to obtain

[1] We use the public master branch of SKIRT v9, git commit `d762d4b`, publicly available at: https://skirt.ugent.be.
[2] https://skirt.ugent.be/skirt9/class_file_polarized_point_source.html

normalised Stokes parameters for each direction and energy. The source is located at the origin, and the source symmetry axis is tilted by $\Delta i = -27.5^\circ$ in the azimuthal plane, such that the accretion-disk axis is always observed at 55° when the binary system is observed at $i = 27.5^\circ$, as discussed in Sect. 2.1.

3.2. Focussed-wind transfer medium in SKIRT

The SKIRT code has various interfaces for importing tabulated transfer media (see e.g. Baes et al. 2024a,b, 2025; Gebek et al. 2024, 2025; Matsumoto et al. 2024, 2025; Kapoor et al. 2024, for recent examples). In this work, we have a 2D model representing the axisymmetric 3D density distribution of the Cyg X-1 system (Sect. 2.2), tabulated on a Cartesian grid in the azimuthal plane. This can be imported as a transfer medium in SKIRT using the `CylindricalCellGeometry` class[3], which has the capability to 'revolve' a tabulated 2D density distribution around a cylindrical symmetry axis (here: the x-axis) to obtain a 3D transfer medium.

The reason for employing the `CylindricalCellGeometry`, which only loads the (normalised) 3D geometry, instead of the `CylindricalCellMedium`, which imports the gas mass density in physical units, is that the latter cannot be rotated. In SKIRT, cylindrical imports always place the cylindrical symmetry axis along the z-axis. However, this z-axis also defines the inclination angle of the observer and the reference direction for polarisation. Without further rotation, this would complicate our analysis: (i) the inclination in SKIRT would not correspond to the inclination of the binary orbit, and (ii) recorded Stokes vectors would not be defined relative to the projected orbital axis. This is resolved by combining the `CylindricalCellGeometry` with a `RotateGeometryDecorator`, with `eulerBeta` = 90°, which rotates the medium back to the $x - y$ plane, and `eulerGamma` = 90°, which realigns the companion with the positive x-axis (Fig. 2).

To obtain the gas mass normalisation for the (normalised) `CylindricalCellGeometry`, we run a single simulation with the corresponding `CylindricalCellMedium`, which loads the gas mass density in physical units; the resulting normalisation is extracted from the convergence information file and applied to the (rotated) `CylindricalCellGeometry` component.

X-ray interactions in the binary medium are implemented in the `XRayAtomicGasMix`, which models absorption, scattering, and fluorescent re-emission by cold gas with X-ray polarisation support. We adopt Wilms et al. (2000) abundances, with a total gas mass of 2.35×10^{-24} g per H-atom, consistent with previous studies of Cyg X-1 (Grinberg et al. 2015; Lai et al. 2024).

Closer to the X-ray source, we assume that the wind is fully ionised, as discussed in Sect. 2.2 (see also Grinberg et al. 2015). In the ionised region (marked in orange on Fig. 2) we adopt the `ElectronMix` with 1.20 free electrons per H-atom, modelling electron scattering with polarisation support, without absorption or fluorescent re-emission.

3.3. General radiative transfer setup

The `RotateGeometryDecorator` mentioned in Sect. 3.2 could have actively rotated the binary medium as a function of orbital phase[4]. Instead, we adopt the co-rotating binary frame, and vary the observer direction and source symmetry axis, which allows the SKIRT medium to be discretised on a spatial grid that closely follows the tabulated focussed-wind model (Sect. 2.2). We adopt a 3D Cartesian grid covering -9.15×10^{10} to 7.33×10^{10} m in 300 steps in the x-direction and -8.24×10^{10} to 8.24×10^{10} m in 300 steps in the y- and z-directions, which corresponds to a uniform spatial resolution of 5.49×10^{8} m in each direction.

Simulation results are recorded for an observer at 2.22 kpc, with $i = 27.5^\circ$ (Miller-Jones et al. 2021) and an azimuthal angle of $(360^\circ \times \texttt{phase}) \pmod{360^\circ}$ in the co-rotating frame. This corresponds to the phase convention of Gies & Bolton (1986b), where phase zero is defined as the inferior conjunction of the companion star, and to an orbital angular momentum vector pointing away from the observer (i.e., clockwise orbital motion on the sky; Miller-Jones et al. 2021). We run a total number of 41 SKIRT simulations, covering one full orbit in 41 phase steps of 0.025. We note that a single simulation with multiple observers cannot provide all radiative transfer results at once, as the relative orientation of the source symmetry axis and the binary medium varies as a function of orbital phase (Sects. 2.1 and 3.1).

Integrated fluxes and surface brightness maps are produced in three energy bands (2 – 4 keV, 4 – 6 keV, and 6 – 8 keV), while spectra are recorded on a logarithmic energy grid that covers the 1 – 100 keV range in 500 bins ($E/\Delta E = 108$). Surface brightness maps are centred on the primary X-ray source, and cover a field of view of 10^{11} m $\times\ 10^{11}$ m in the sky-projected Cyg X-1 frame. All SKIRT instruments (i.e., broadband, spectral, and imaging) can separate the individual flux contributions of the direct source emission, the electron-scattered continuum, and the fluorescent lines, which provides valuable information for the analysis of the radiative transfer results (Sect. 4).

The X-ray source emission and all radiative processes are modelled up to 200 keV, as required to achieve fully converged X-ray flux and polarisation spectra up to ∼100 keV (see Vander Meulen et al. 2023, for a discussion). The number of discrete photon packets launched from the kerrC point source is 5×10^{8}, which offers an optimal balance between simulation runtime and Monte Carlo noise.[5] Each individual simulation has a runtime of about 35 hours on a single CPU core; on a small 41-core cluster, the full set of 41 simulations completes in roughly 35 hours when run in parallel, totalling about 1,435 core-hours.

4. Results and discussion

4.1. Radiative transfer results

Figure 3 shows the simulated Stokes I surface brightness maps in the 4 – 6 keV band at eight equally-spaced orbital phases, providing a direct view on the Cyg X-1 system over one orbit. Throughout the orbit, the observed emission is dominated by the direct contribution from the point-like X-ray source (Sect 2.1), while the extended emission traces reflection off the companion star and its stellar wind (Sect 2.2). The extended emission region rotates about the line of sight with the binary orbit (Fig. 3), and contributes most near phase 0.5, when the focussed wind and the illuminated face of the companion star are maximally exposed. Similar maps were obtained for the 2–4 keV and 6–8 keV bands: at lower energies the diffuse scattered emission dominates, while

[3] https://skirt.ugent.be/skirt9/class_cylindrical_cell_geometry.html

[4] Varying `eulerGamma` as $(90^\circ + 360^\circ \times \texttt{phase}) \pmod{360^\circ}$, which corresponds to the standard phase convention of Gies & Bolton (1986b), with the orbit appearing clockwise on the sky (Miller-Jones et al. 2021). We note that the rotation decorator implements a passive coordinate transformation, equivalent to an active rotation by the opposite angle.

[5] These 5×10^{8} photons do not just escape the model in all directions, with a low probability of being detected, but instead contribute directly to the simulation output at each (re)emission and scattering location through peel-off (see Yusef-Zadeh et al. 1984).

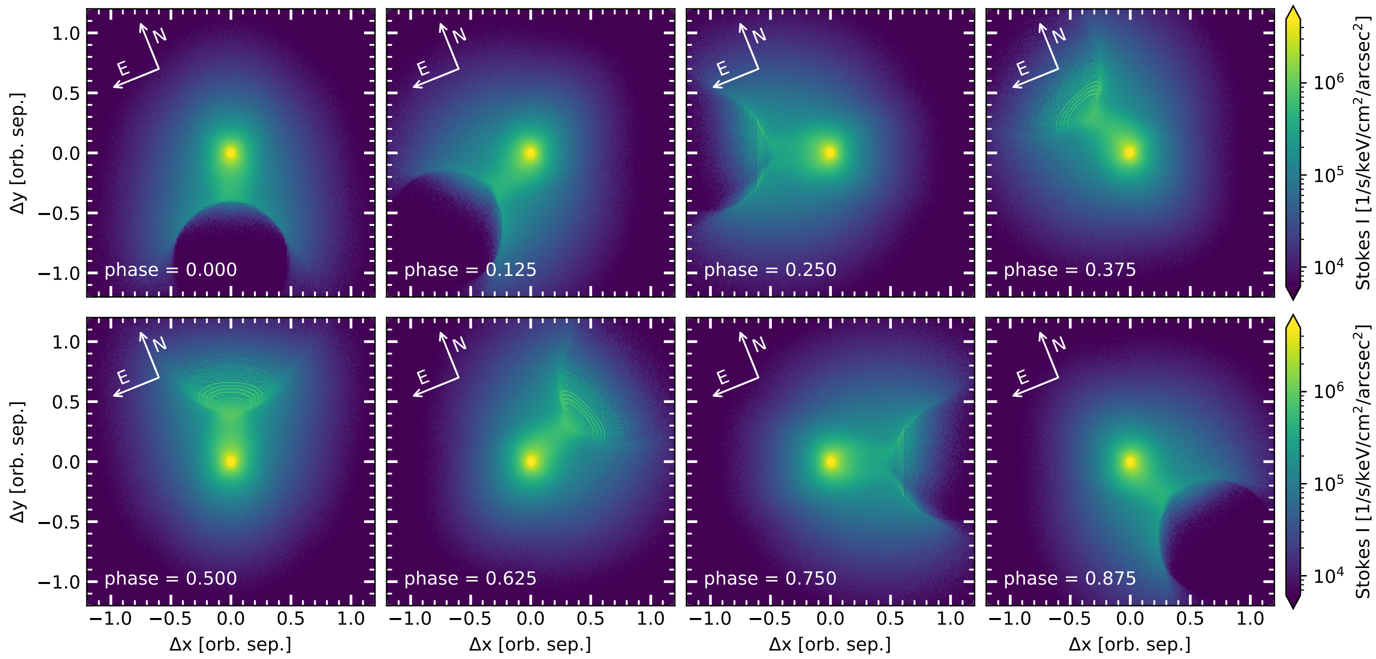

Fig. 3. Broadband Stokes I surface brightness maps in the 4 – 6 keV band at eight equally-spaced orbital phases, providing a direct view of the Cyg X-1 system over one orbit. The binary orbit is observed at $i = 27.5°$, with the orbital angular momentum vector pointing away from the observer, and phase zero corresponding to the inferior conjunction of the companion star. The projected accretion-disk axis is aligned with the positive y-direction, which corresponds to a rotation of 21° relative to celestial north (indicated on each panel; Sect. 4.6). The primary X-ray source is centred at (0, 0), and the extended emission traces reflection off the companion star and its focussed stellar wind (Sect. 2.2).

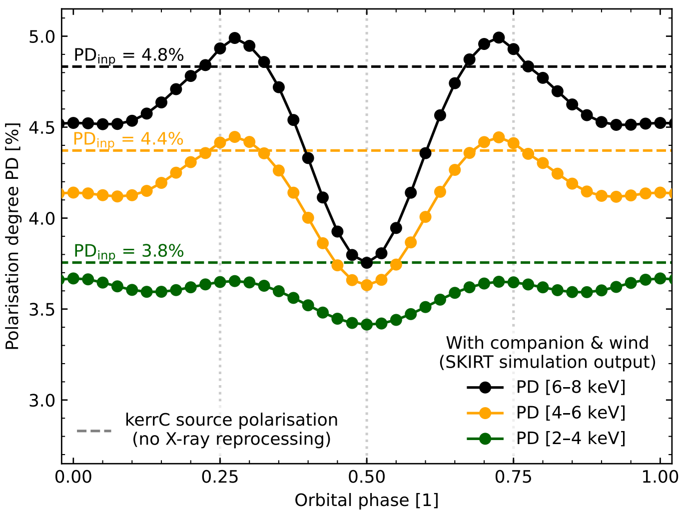

Fig. 4. Orbital modulation of the linear polarisation degree PD in three energy bands. The dashed horizontal lines indicate the intrinsic source polarisation in each band (PD$_{inp}$ from kerrC; Fig. 1).

reflection off the companion star and the focussed stellar wind becomes increasingly important at higher energies.

Our main result is shown in Fig. 4: the linear polarisation degree PD as a function of orbital phase, in three energy bands (2 – 4 keV, green; 4 – 6 keV, orange; 6 – 8 keV, black). We find a prominent double-peaked polarisation modulation, with a peak-to-peak PD amplitude of 0.25, 0.81, and 1.24 percentage points in the three energy bands, respectively, which corresponds to a substantial modulation of the source polarisation degree (7%, 19%, and 26%). The modulation is symmetric about phase 0.5, with an energy-dependent amplitude, but otherwise similar phase dependence across all bands; PD is minimal at phase 0.5, when the companion lies behind the X-ray source, and maximal near phases 0.275 and 0.725, when the binary components are roughly side-by-side (Fig. 3). The dashed horizontal lines indicate the intrinsic source polarisation in each band (PD$_{inp}$ = 3.8%, 4.4%, and 4.8%; Fig. 1). X-ray reprocessing generally reduces the observed PD, with the exception of a small amplification near phases 0.275 and 0.725 in the highest energy bands.

The linear polarisation degree at each orbital phase (Fig. 4) was calculated from the simulated broadband I, Q, and U fluxes, which are shown in Fig. 5 (top row) for the 6−8 keV band, which is the energy band where the PD modulation is most prominent. For each Stokes parameter, the total flux (red) is the sum of three distinct flux contributions: the direct source emission (green), the Compton-scattered continuum (orange), and the fluorescent-line emission (blue); $I_{tot} = I_{dir} + I_{sca} + I_{fluo}$, and equivalently for Q and U. The intrinsic source flux is shown in grey as a reference.

The total Stokes I flux (Fig. 5a, red) is dominated by the direct source contribution (green), as expected for the modest line-of-sight extinction of Cyg X-1 (Grinberg et al. 2015). In the 6 – 8 keV band, the intrinsic source flux is transmitted at 94 – 98%, depending on the orbital phase: the optical depth is minimal at phase 0.5 ($\tau_{ext} = 0.020$), when the companion lies behind the X-ray source, and maximal at phase 0 ($\tau_{ext} = 0.065$), when the line of sight traverses the largest column of stellar wind. The same trend is apparent in Q_{dir} (Fig. 5b, green), while $U_{dir} \approx 0$ by definition (Sect. 2.1). Since extinction attenuates I and Q by the same factor, both the Q/I ratio and PD of the direct flux contribution remain unchanged at PD$_{inp}$ = 4.8% throughout the orbit[6] (Fig. 5f, green); the direct flux varies, but introduces no polarisation modulation.

[6] This is not generally true, as energy-dependent extinction could alter the flux-weighted broadband PD of the direct contribution. This effect is

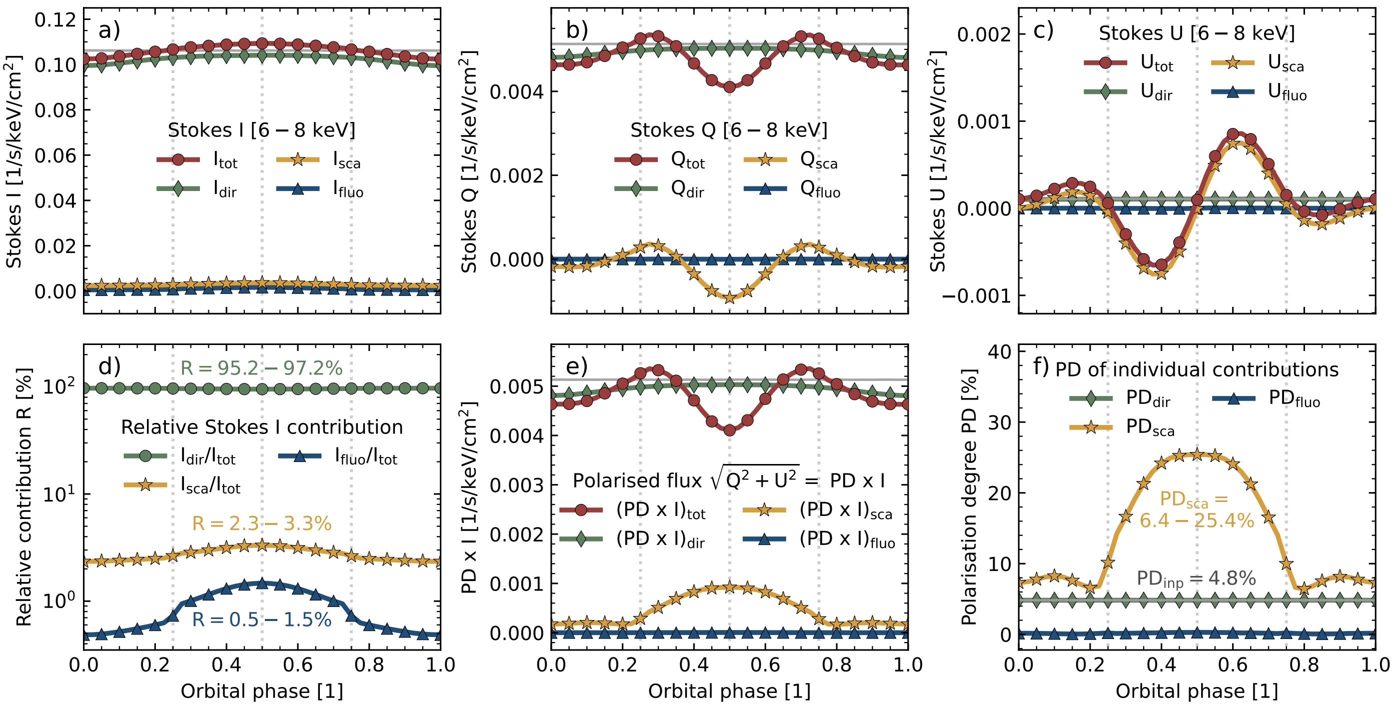

Fig. 5. Broadband Stokes I, Q, and U fluxes as a function of orbital phase for the 6 – 8 keV band. The total observed flux (red) is the sum of three flux contributions: the direct source contribution (green), the Compton-scattered continuum (orange), and the fluorescent-line emission (blue); $I_{tot} = I_{dir} + I_{sca} + I_{fluo}$, and equivalently for Stokes Q and U. The intrinsic primary-source flux is shown in grey as a reference. Stokes Q and U are referred to the projected accretion-disk axis, which is offset from celestial north by 21° (see Fig. 3 and Sect. 4.6).

A fraction of the source flux absorbed within the binary system is re-emitted as fluorescent line emission (Fig. 5a, blue). As fluorescent lines are intrinsically unpolarised ($PD_{fluo} = 0$, and hence $Q_{fluo} = U_{fluo} = 0$; Fig. 5b,c,f), they do not contribute to the polarised flux (Fig. 5e), and only dilute the total polarisation degree. However, as their relative Stokes I contribution is only 0.5 – 1.5% (Fig. 5d), this dilution is negligible, and fluorescent line emission can be ignored in the polarisation analysis.

The remaining flux contribution is the Compton-scattered continuum (Fig. 5, orange). As neither the direct flux (constant PD_{dir} at 4.8%) nor the fluorescent line emission (negligible flux) drives a polarisation modulation, the observed PD modulation must originate entirely from the Compton-scattered continuum, which is discussed in detail in Sect. 4.2.

4.2. Polarisation of the Compton-scattered continuum

While the Compton-scattered continuum flux contributes only 2.3 – 3.3% of the total Stokes I flux (Fig. 5d, orange), this component is highly polarised (up to 25%; Fig. 5f) and therefore contributes notably to the total polarised flux (PD × I; Fig. 5e). Two scattering regions can be identified: (i) a diffuse scattering halo centred on the X-ray source, which is visible throughout the orbit; and (ii) a more distant component from scattering off the companion star and its focussed stellar wind, which dominates when the illuminated face of the companion and the focussed-wind axis are exposed, between phases 0.25 and 0.75 (Fig. 3).

These two scattering regions contribute differently to the net spatially integrated polarisation. The diffuse stellar wind close to the X-ray source provides a nearly isotropic scattering medium, whose polarisation contributions largely cancel in the integrated flux, yielding a low net PD_{sca} of 6 – 8% (Fig. 5f; not exactly zero due to the anisotropic illumination of the scattering medium by the X-ray source, see Fig. 1). The companion surface and the focussed wind, by contrast, constitute an anisotropic scattering medium along the donor-black hole axis, inducing significant net polarisation in the spatially integrated flux (up to 25%; Fig. 5f). This is apparent in the polarised flux $(PD{\times}I)_{sca}$ (Fig. 5e, orange), which peaks between phases 0.25 and 0.75.

The total polarised flux does not only depend on the magnitude of the polarised flux contributions, but also on the relative orientation of their polarisation directions. The polarisation direction of the scattered flux is set by the geometry of the scattering medium: since the scattered polarised flux is dominated by single scattering off the companion star and the focussed wind along the donor-black hole axis, and single scattering induces polarisation perpendicular to the scattering plane (e.g., Vander Meulen et al. 2024), the net scattered polarisation is perpendicular to the sky-projected donor-black hole axis. As this sky-projected axis sweeps about the line of sight throughout the orbit, the scattered polarisation direction rotates with orbital phase.[7] This is visualised in Fig. 6, showing the linear polarisation maps in the 6 – 8 keV band, derived from the simulated Stokes I, Q, and U surface brightness maps.

The total polarised flux is dominated by the direct source contribution (Sect. 4.1), which is polarised along the projected accretion disk axis (Sect. 2.1; positive *y*-direction in Fig. 6). As the scattered polarisation direction rotates with orbital phase, it alternately reinforces and counteracts the direct source polari-

negligible here (|ΔPD| < 0.04%, 0.004%, and 0.0004%, respectively), as the source PD_{inp} is roughly constant with energy (Fig. 1, bottom).

[7] At $i = 27.5°$, the projected axis does not rotate uniformly: the phase offset relative to uniform motion is zero at phases 0, 0.25, 0.5, and 0.75, and reaches a maximum offset of |Δphase| = 0.009 when the projected binary axis lies diagonally (Fig. 3); this projection effect is negligible and does not notably affect the observed polarisation modulation.

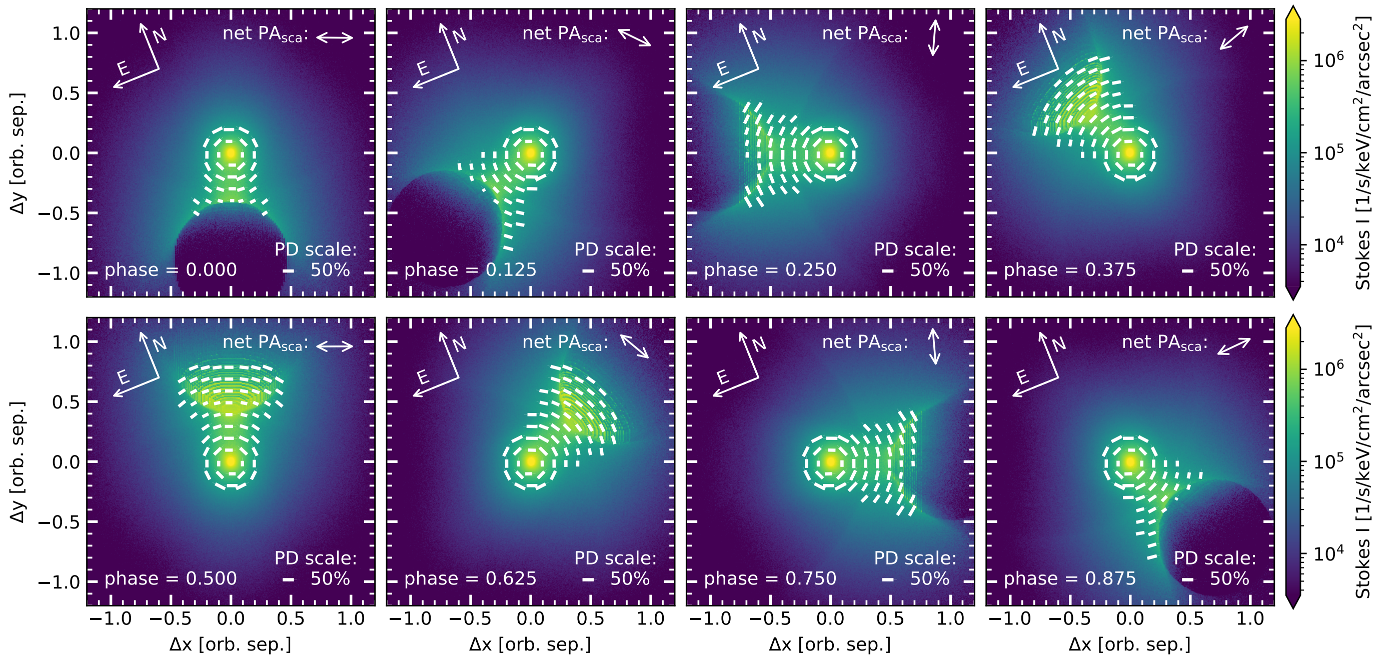

Fig. 6. Linear polarisation maps in the 6 – 8 keV band at eight equally-spaced orbital phases (see Fig. 3 for more details). The spatially resolved polarisation degree PD and polarisation angle PA are represented by the length and orientation of the white line segments, respectively. The direct source polarisation is aligned with the projected accretion-disk axis (positive y-direction), which is offset from celestial north by 21° (see Fig. 3 and Sect. 4.6); the net scattered polarisation direction is indicated on each panel and rotates with orbital phase.

sation, modulating the total polarised flux. At phases 0.25 and 0.75, the two polarisation directions align (Fig. 6), and the scattered flux amplifies the observed polarisation degree (Fig. 4). At phases 0 and 0.5, they are perpendicular (Fig. 6), and the scattered flux counteracts the direct source polarisation, reducing the observed PD. This alternating (mis)alignment repeats twice per orbit, naturally producing the double-peaked $P_{orb}/2$ polarisation modulation (Fig. 4).

The detailed shape of the polarisation modulation is further set by the phase-dependent magnitude of the scattered polarised flux $(\mathrm{PD} \times \mathrm{I})_{sca}$ (Fig. 5e, orange). This peaks near phase 0.5, when the illuminated face of the companion star is maximally exposed, resulting in a deeper PD minimum at phase 0.5 than at phase 0 (Fig. 4). Similarly, the PD maxima are shifted from phases 0.25 and 0.75 with perfect alignment to phases 0.275 and 0.725 where the scattered polarised flux is larger.

4.3. Visualisation in the Q – U plane

This interplay between the direct and scattered polarised flux is most clearly visualised in the Q – U plane (Fig. 7). The Stokes Q and U parameters describe the polarised flux along two pairs of reference axes, such that orthogonal polarisation directions carry opposite signs and cancel when added: positive Q-values describe polarisation along the sky-projected accretion-disk axis (i.e., the source polarisation direction; Sect. 4.6), while negative Q-values describe polarisation perpendicular to this axis; Stokes U similarly describes polarisation along orthogonal axes rotated by 45° (see e.g. Peest et al. 2017).

The direct contribution traces a nearly constant positive-Q locus (Fig. 7, diamonds), with a minor symmetric variation about phase 0.5 due to the variable line-of-sight extinction (Sect. 4.1). The scattered contribution (Fig. 7, stars) rotates twice about the origin throughout the orbit, with the polarised flux distributed sinusoidally between Q_{sca} and U_{sca} (Fig. 5b,c); the larger loop corresponds to phases 0.25 – 0.75, when the illuminated face of the companion is exposed. The total polarisation signal (Fig. 7, circles) is the vector sum of these two contributions, and reflects the rotation of the scattered polarised flux about the direct source polarisation signal in the Q – U plane.

The total polarised flux $(\mathrm{PD} \times \mathrm{I})_{tot}$ is the vector norm of $(\mathrm{Q}_{tot}, \mathrm{U}_{tot}) = (\mathrm{Q}_{dir} + \mathrm{Q}_{scat}, \mathrm{U}_{scat})$. Since the U_{sca} component is orthogonal to the dominant $(\mathrm{Q}_{dir}, 0)$ contribution in the Q – U plane (Fig. 7), the total polarised flux is to first order insensitive to the U_{sca} signal: $(\mathrm{PD} \times \mathrm{I})_{tot} \approx \mathrm{Q}_{dir} \times [1 + 2\,\mathrm{Q}_{sca}/\mathrm{Q}_{dir}]^{1/2}$. The observed PD modulation (Fig. 4) therefore closely resembles the orbital trend of Q_{sca} (Fig. 5b, orange).

Similarly, the effect of U_{sca} on the observed net polarisation angle PA is minor, since $|\mathrm{U}_{sca}| \ll \mathrm{Q}_{tot}$ (Fig. 7). Still, as $\mathrm{U}_{dir} \approx 0$ and Q_{tot} lies along the positive Q-direction, U_{sca} is the only flux contribution that can alter PA, and therefore we expect a minor PA modulation centred on PA = 0°. This can be visualised in the Q – U plane (Fig. 7), where PA corresponds to 1/2 of the angle between $(\mathrm{Q}_{tot}, \mathrm{U}_{tot})$ and the positive Q-direction. Fig. 8 shows our predicted modulation of the polarisation angle, with $|\Delta\mathrm{PA}| < 4.6°$ throughout the orbit, consistent with observational studies reporting no significant variation in PA with orbital phase (Krawczynski et al. 2022; Steiner et al. 2024; Kravtsov et al. 2025). Specifically, we find a peak-to-peak PA amplitude of 2.2°, 6.6°, and 9.1° in the 2−4, 4−6, and 6−8 keV bands, respectively. To first order, $\Delta\mathrm{PA} \approx 0.5 \times \mathrm{U}_{sca}/\mathrm{Q}_{dir}$, tracing the orbital trend of U_{sca} (Fig. 5c, orange), which is antisymmetric about phase 0.5.

4.4. Energy dependence of the polarisation modulation

The previous subsections focussed on the 6 – 8 keV band, which exhibits the most prominent polarisation modulation (Fig. 4), with a peak-to-peak PD amplitude of 1.24 percentage points,

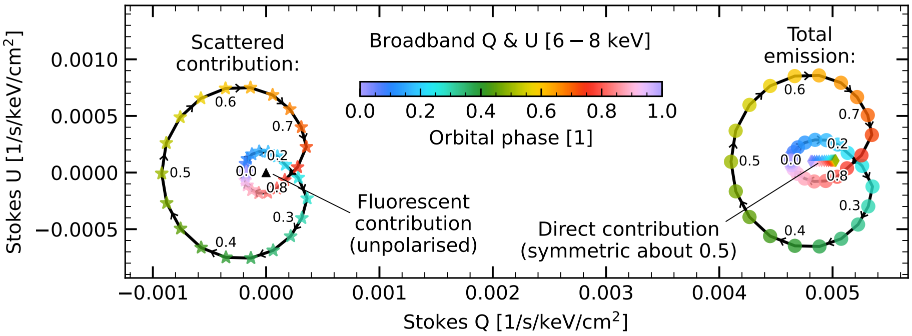

Fig. 7. Variation of the broadband Stokes Q and U fluxes in the 6 − 8 keV band with orbital phase. The total observed flux is the sum of the direct source emission, the reflected emission, and the (unpolarised) fluorescent line emission. The Q-axis is aligned with the primary source polarisation direction (Sect. 4.6).

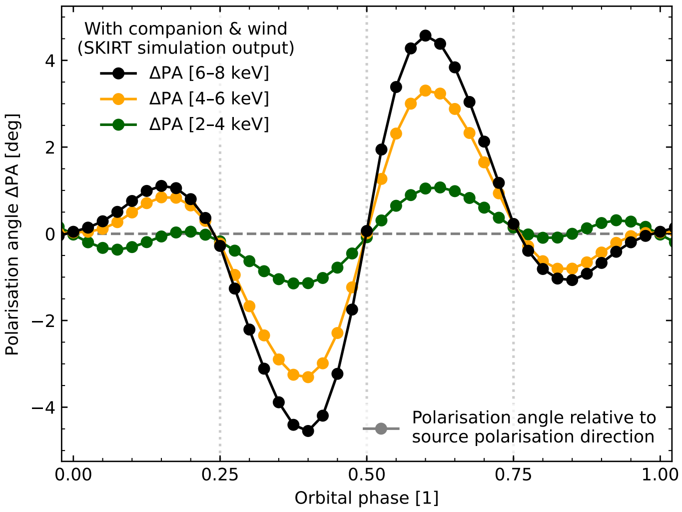

Fig. 8. Orbital modulation of the polarisation angle offset, ΔPA, in three energy bands, relative to the intrinsic source polarisation direction.

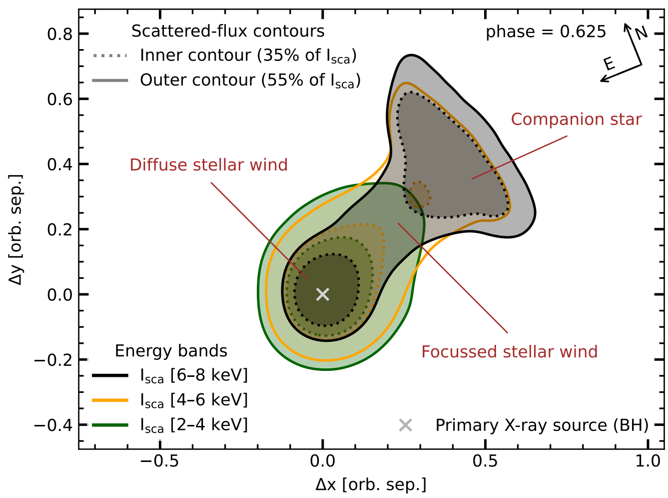

Fig. 9. Energy dependence of the extended scattered-flux region: with increasing energy, the dominant scattering region shifts from the diffuse stellar wind close to the X-ray source (green) to the focussed stellar wind and companion star surface (black). The inner and outer contours encircle 35% and 55% of the scattered flux I_{sca}, respectively.

compared to 0.81 and 0.25 in the 4 − 6 and 2 − 4 keV bands, respectively. The modulation strength increases with energy, a trend that continues beyond the IXPE range and reaches 3.80 percentage points in the *XL-Calibur* band (19 − 64 keV).

This energy dependence reflects the growing influence of the scattered flux on the total observed polarisation signal as energy increases. First, the scattered emission travels longer distances through the binary medium than the direct source emission, and is therefore disproportionately suppressed by photo-absorption; as the absorption efficiency drops steeply across the 2 − 8 keV band (e.g. Vander Meulen et al. 2023), the scattered-to-direct flux ratio rises. Since the PD modulation originates entirely from the scattered flux (with $PD_{dir} = PD_{inp}$ constant; Sect. 4.1), the modulation amplitude scales with this flux ratio, and therefore grows with energy.

Second, a similar reasoning holds for the two spatial regions that contribute to the scattered flux: (i) the diffuse scattering halo centred on the X-ray source, which induces low net polarisation, and (ii) the more distant reflection off the companion star and the focussed stellar wind, which drives the prominent double-peaked PD modulation (Sect. 4.2). As the latter region corresponds to longer paths through parts of the binary medium that are also denser, it is more strongly attenuated by photo-absorption; its relative contribution therefore rises with energy, reinforcing the PD modulation beyond the rising scattered-to-direct flux ratio. This is visualised in Fig. 9: across the IXPE band, the scattered flux progressively shifts from the central scattering halo to the more distant companion star surface with increasing energy.

4.5. Reduction of the phase-averaged polarisation degree

Finally, we address why the phase-averaged polarisation degree is reduced relative to the intrinsic source polarisation (Sect. 4.1). This reduction amounts to 0.17, 0.22, and 0.28 percentage points in the 2 − 4, 4 − 6, and 6 − 8 keV bands, relative to PD_{inp} = 3.8%, 4.4%, and 4.8%, respectively. In relative terms, the polarisation degree is reduced by a notable 5%, 5%, and 6%.

First, the anisotropic X-ray source (Fig. 1) disproportionately illuminates the polar regions of the diffuse stellar wind, inducing a net polarisation signal perpendicular to the source polarisation direction. As the diffuse scattering halo is visible at all orbital phases (Fig. 3), this signal persistently counteracts the source polarisation, reducing the phase-averaged PD.

Second, the distant-reflection contribution (driving the main polarisation modulation) peaks when the illuminated face of the companion star is maximally exposed (near phase 0.5; Fig. 5e). At this phase, the reflection-induced polarisation signal counteracts the source polarisation (Fig. 6). Near phases 0.25 and 0.75, where the source polarisation is amplified, the polarised flux is much weaker, so the net reduction near phase 0.5 dominates the phase average. Moreover, the distant reflection contributes a strictly positive Stokes I flux at every orbital phase (Fig. 5d), diluting the phase-averaged polarisation degree even when the polarised flux modulation partially cancels.

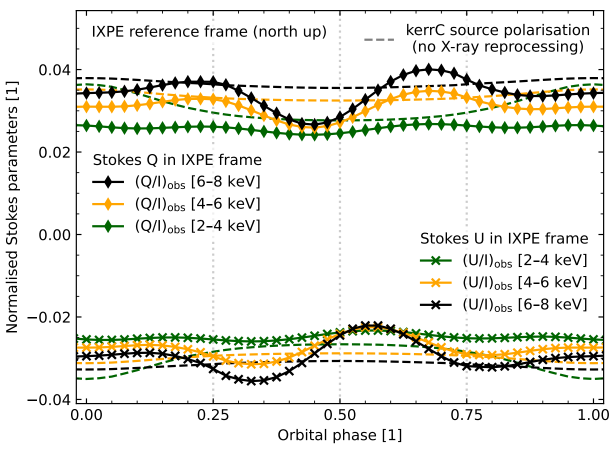

Fig. 10. Normalised Stokes parameters $(Q/I)_{obs}$ and $(U/I)_{obs}$ in the IXPE reference frame (celestial north up), accounting for the 21° roll angle between the projected accretion-disk axis and celestial north (Sect. 4.6).

4.6. Stokes parameters in the IXPE reference frame

Throughout this work, we have oriented the observer such that the sky-projected accretion-disk axis points along the positive *y*-direction. This choice has greatly simplified our analysis: the source polarisation aligns with the positive Stokes Q-direction, and the PD and PA modulations trace Q_{sca} and U_{sca}, respectively (Sect. 4.3).

IXPE observations, however, are referred to celestial north. As the projected accretion-disk axis of Cyg X-1 is offset from north by 21° towards the west (Krawczynski et al. 2022), the observed Stokes Q_{obs} and U_{obs} parameters are obtained by rotating Q_{tot} and U_{tot} (Fig. 5b,c, red) around the line of sight:

$$Q_{obs} = \cos(2\times 21^\circ)\, Q_{tot} + \sin(2\times 21^\circ)\, U_{tot}, \quad (1a)$$

$$U_{obs} = -\sin(2\times 21^\circ)\, Q_{tot} + \cos(2\times 21^\circ)\, U_{tot}. \quad (1b)$$

The normalised $(Q/I)_{obs}$ and $(U/I)_{obs}$ parameters are shown in Fig. 10, which can be directly compared to the Stokes Q and U parameters as measured by IXPE. We note that the main results of this work, the PD and ΔPA modulations (Figs. 4 and 8), are invariant under this change of reference direction.

5. Summary and outlook

This work presents a 3D radiative transfer model for Cyg X-1, combining a detailed description of the polarised X-ray source emission (Sect. 2.1) with a focussed stellar wind model for the binary medium (Sect. 2.2). Using the 3D X-ray radiative transfer code SKIRT (Vander Meulen et al. 2023, 2024), we model X-ray reprocessing in the system, and simulate broadband Stokes I, Q, and U fluxes, surface brightness maps, and polarisation maps over one binary orbit, to quantify the reflection-induced PD and PA variations as a function of orbital phase and photon energy.

We find a prominent double-peaked ($P_{orb}/2$) polarisation modulation, with a peak-to-peak PD amplitude of 0.25, 0.81, and 1.24 percentage points in the 2 – 4, 4 – 6, and 6 – 8 keV bands, respectively, which corresponds to a substantial modulation of the source polarisation degree (7%, 19%, and 26%; Fig. 4). The PA modulation is more modest, with $|\Delta PA| < 4.6^\circ$ (Fig. 8). Yet, this PA modulation could constrain the sense of the orbital rotation of Cyg X-1, which is currently established only through interferometric radio astrometry (Miller-Jones et al. 2021, and references therein); an independent confirmation through X-ray polarimetry would be valuable.

The polarisation modulation originates from reflection off the companion star and the focussed stellar wind (Sect. 4.2), whose reflection-induced polarisation signal is perpendicular to the donor-black hole axis (Fig. 6), and rotates with the binary orbit, alternately reinforcing and counteracting the direct source polarisation. This naturally produces the double-peaked $P_{orb}/2$ periodicity (Fig. 4). The PD modulation amplitude increases with energy (Sect. 4.4), which is related to the penetrating power of the X-ray photons: as the modulation arises from reflection off the distant star and wind, which corresponds to longer and denser paths through the binary medium, the distant-reflection signal is more prominent at higher energies, where the extinction is lower. The bulk of the scattered flux shifts from the central scattering halo (low PD) to the distant companion star surface (high PD) with increasing energy (Fig. 9).

Crucially, X-ray reflection also reduces the phase-averaged polarisation degree relative to the intrinsic source polarisation, by 5%, 5%, and 6% in the three energy bands (Sect. 4.5). This is because reflection off the diffuse stellar wind counteracts the source polarisation at all phases, and because the distant-reflection contribution (i.e., the main polarisation modulation) peaks when counteracting the source polarisation (Fig. 6). We note that such reduction should be accounted for in all wind-fed X-ray binaries, where reflection within the binary system is expected to systematically lower the observed polarisation. For BHXBs, this reduction further increases the tension between the unexpectedly high PDs measured by IXPE and those predicted by theoretical disk-corona models (Krawczynski et al. 2022).

This work predicts a polarisation modulation with a period of $P_{orb}/2$, induced by reflection off the companion star and its wind. Kravtsov et al. (2025) recently reported tentative evidence for a PD modulation with the orbital period P_{orb}, but did not quantify the amplitude of any modulation at $P_{orb}/2$. They analysed the full 2 – 8 keV band, which is dominated by the 2 – 4 keV flux, where we predict a $P_{orb}/2$ modulation amplitude (peak-to-peak) of only 0.25 percentage points (Fig. 4), which is well below the uncertainties of the IXPE data. Our predictions therefore do not contradict the observational results of Kravtsov et al. (2025).

Moreover, we note that the intrinsic source polarisation of Cyg X-1 varies with accretion state, on timescales comparable to the orbital period (Tananbaum et al. 1972; Pottschmidt et al. 2003; Done et al. 2007; Grinberg et al. 2013); these intrinsic variations can mask or mimic the reflection-induced PD and PA modulations, complicating a detection. In a forthcoming paper, we confront our predictions with the accumulated IXPE data, by analysing the phase-dependent polarisation measurements in three energy bands and isolating the orbital signal from spectral-state variations, to constrain the reflection-induced modulation and its detectability with IXPE.

The SKIRT simulations presented in this work generated a large, quantitative dataset of phase-resolved Stokes I, Q, and U broadband fluxes, spectra, and surface brightness maps over the 1 – 100 keV range. This enables a range of follow-up studies, including spatially resolved and spectral analyses, and extensions to higher-energy bands such as *XL-Calibur* (19 – 64 keV; Abarr et al. 2021). Furthermore, it provides a theoretical basis for the interpretation of ongoing IXPE campaigns on BHXBs, and quantitative predictions for current and future X-ray spectro-polarimetric missions.

Our radiative transfer model for Cyg X-1 can be extended in several directions. First, the stellar wind of HDE 226868 is highly structured (Owocki & Rybicki 1984; Grinberg et al. 2015; Sundqvist et al. 2018; Hirsch et al. 2019). Wind clumping is readily incorporated into SKIRT (see e.g. Stalevski et al. 2016), but disentangling its polarisation signature warrants a dedicated study, and is deferred to future work. Second, the current model considers only the wind density distribution; the corresponding velocity field can also be imported in SKIRT (Camps & Baes 2020), introducing velocity shifts and broadening that are below the spectral resolution of IXPE, but are directly accessible with XRISM/Resolve spectroscopy (Tashiro et al. 2025). Finally, a more detailed treatment of the ionisation structure is foreseen with the forthcoming SKIRT release of X-ray radiative transfer in partially ionised gas.

The presented framework can also be applied to Cyg X-1 in the soft (or intermediate) accretion state, or could be extended to other wind-fed X-ray binaries, such as the neutron-star systems Vela X-1 and Cen X-3. All simulation elements used in this work (such as the interfaces for importing custom sources and transfer media) are built into the public master branch of the SKIRT code, which is publicly available and well documented[8]. We warmly invite the community to use the code in any way they see fit.

Acknowledgements. B. V. acknowledges support through the European Space Agency (ESA) Research Fellowship in Space Science, and thanks Ghent University and SRON for their hospitality throughout the course of this work. K. H. and H. K. thank NASA for support under the grants 80NSSC24K1178, 80NSSC24K1749, and 80NSSC24K1819, and acknowledge support from the McDonnell Center for the Space Sciences at Washington University in St. Louis. They furthermore acknowledge the use of the High Performance Computing cluster of the WashU Physics Department maintained by S. Iyer.

References

Abarr, Q., Awaki, H., Baring, M. G., et al. 2021, Astroparticle Physics, 126, 102529
Ahlberg, V., Kravtsov, V., & Poutanen, J. 2024, A&A, 688, A220
Awaki, H., Baring, M. G., Bose, R., et al. 2025, ApJ, 994, 37
Baes, M., Gebek, A., Kunene, S., et al. 2025, A&A, 696, A52
Baes, M., Gebek, A., Trčka, A., et al. 2024a, A&A, 683, A181
Baes, M., Mosenkov, A., Kelly, R., et al. 2024b, A&A, 683, A182
Bałucińska-Church, M., Church, M. J., Charles, P. A., et al. 2000, MNRAS, 311, 861
Beloborodov, A. M. 1998, ApJ, 496, L105
Boroson, B. & Vrtilek, S. D. 2010, ApJ, 710, 197
Brigitte, M., Hadrava, P., Kubátová, B., et al. 2025, A&A, 695, A115
Brown, J. C., McLean, I. S., & Emslie, A. G. 1978, A&A, 68, 415
Camps, P. & Baes, M. 2015, Astronomy and Computing, 9, 20
Camps, P. & Baes, M. 2020, Astronomy and Computing, 31, 100381
Castor, J. I., Abbott, D. C., & Klein, R. I. 1975, ApJ, 195, 157
Done, C., Gierliński, M., & Kubota, A. 2007, A&A Rev., 15, 1
Dovčiak, M., Podgorný, J., Svoboda, J., et al. 2024, Galaxies, 12, 54
Draghis, P. A., Miller, J. M., Kara, E., et al. 2025, arXiv e-prints, arXiv:2511.17338
El Mellah, I., Sander, A. A. C., Sundqvist, J. O., & Keppens, R. 2019, A&A, 622, A189
Friend, D. B. & Castor, J. I. 1982, ApJ, 261, 293
Gebek, A., Diemer, B., Martorano, M., et al. 2025, A&A, 695, A90
Gebek, A., Trčka, A., Baes, M., et al. 2024, MNRAS, 531, 3839
Gies, D. R. & Bolton, C. T. 1986a, ApJ, 304, 389
Gies, D. R. & Bolton, C. T. 1986b, ApJ, 304, 371
Gies, D. R., Bolton, C. T., Blake, R. M., et al. 2008, ApJ, 678, 1237
Gies, D. R., Bolton, C. T., Thomson, J. R., et al. 2003, ApJ, 583, 424
Grinberg, V., Hell, N., Pottschmidt, K., et al. 2013, A&A, 554, A88
Grinberg, V., Leutenegger, M. A., Hell, N., et al. 2015, A&A, 576, A117
Hanke, M., Wilms, J., Nowak, M. A., et al. 2009, ApJ, 690, 330
Hirsch, M., Hell, N., Grinberg, V., et al. 2019, A&A, 626, A64
Jiang, J. 2024, Galaxies, 12, 80
Kapoor, A. U., Baes, M., van der Wel, A., et al. 2024, A&A, 692, A79
Kravtsov, V., Berdyugin, A. V., Piirola, V., et al. 2020, A&A, 643, A170
Kravtsov, V., Bocharova, A., Veledina, A., et al. 2025, A&A, 701, A115
Krawczynski, H. & Beheshtipour, B. 2022, ApJ, 934, 4
Krawczynski, H. & Hu, K. 2025, ApJ, 993, 54
Krawczynski, H., Muleri, F., Dovčiak, M., et al. 2022, Science, 378, 650
Krawczynski, H., Yuan, Y., Chen, A. Y., et al. 2024, ApJ, 977, L10
Lai, E. V., De Marco, B., Cavecchi, Y., et al. 2024, A&A, 691, A78
Majumder, S., Kushwaha, A., Singh, S., et al. 2026, MNRAS, 545, staf1933
Marra, L., Brigitte, M., Rodriguez Cavero, N., et al. 2024, A&A, 684, A95
Matsumoto, K., Hirashita, H., Nagamine, K., et al. 2024, A&A, 689, A79
Matsumoto, K., Sommovigo, L., Gebek, A., et al. 2025, arXiv e-prints, arXiv:2508.21157
Miller, J. M., Wojdowski, P., Schulz, N. S., et al. 2005, ApJ, 620, 398
Miller-Jones, J. C. A., Bahramian, A., Orosz, J. A., et al. 2021, Science, 371, 1046
Miškovičová, I., Hell, N., Hanke, M., et al. 2016, A&A, 590, A114
Niedzwiecki, A., Szanecki, M., Veledina, A., et al. 2026, arXiv e-prints, arXiv:2603.10870
Owocki, S. P. & Rybicki, G. B. 1984, ApJ, 284, 337
Peest, C., Camps, P., Stalevski, M., Baes, M., & Siebenmorgen, R. 2017, A&A, 601, A92
Pottschmidt, K., Wilms, J., Nowak, M. A., et al. 2003, A&A, 407, 1039
Poutanen, J., Veledina, A., & Beloborodov, A. M. 2023, ApJ, 949, L10
Ramachandran, V., Sander, A. A. C., Oskinova, L. M., et al. 2025, A&A, 698, A37
Rankin, J., Kravtsov, V., Muleri, F., et al. 2024, ApJ, 962, 34
Rodriguez Cavero, N., Marra, L., Krawczynski, H., et al. 2023, ApJ, 958, L8
Sowers, J. W., Gies, D. R., Bagnuolo, W. G., et al. 1998, ApJ, 506, 424
Stalevski, M., Ricci, C., Ueda, Y., et al. 2016, MNRAS, 458, 2288
Steiner, J. F., Nathan, E., Hu, K., et al. 2024, ApJ, 969, L30
Sundqvist, J. O., Owocki, S. P., & Puls, J. 2018, A&A, 611, A17
Tananbaum, H., Gursky, H., Kellogg, E., Giacconi, R., & Jones, C. 1972, ApJ, 177, L5
Tashiro, M., Kelley, R., Watanabe, S., et al. 2025, PASJ
Tomaru, R., Done, C., & Odaka, H. 2024, MNRAS, 527, 7047
Vander Meulen, B., Camps, P., Savić, Đ., et al. 2024, A&A, 689, A297
Vander Meulen, B., Camps, P., Stalevski, M., & Baes, M. 2023, A&A, 674, A123
Weisskopf, M. C., Soffitta, P., Baldini, L., et al. 2022, Journal of Astronomical Telescopes, Instruments, and Systems, 8, 026002
West, A. T. & Krawczynski, H. 2023, ApJ, 957, 9
Wilms, J., Allen, A., & McCray, R. 2000, ApJ, 542, 914
Yamada, S., Hell, N., Costantini, E., et al. 2025, PASJ
Yusef-Zadeh, F., Morris, M., & White, R. L. 1984, ApJ, 278, 186

[8] https://skirt.ugent.be